

Calving of a large Greenlandic tidewater glacier has complex links to meltwater plumes and mélange

Samuel J. Cook^{1,2†}, Poul Christoffersen¹, Martin Truffer³, Thomas R. Chudley¹, Antonio Abellán⁴.

†Corresponding Author (samuel.cook@univ-grenoble-alpes.fr)

¹ Scott Polar Research Institute, University of Cambridge

² Institut des Géosciences de l'Environnement, Université Grenoble Alpes

³ Geophysical Institute, University of Alaska, Fairbanks, USA

⁴ Research Center on the Alpine Environment, Valais, Switzerland

Key Points:

- We derive a record of 8,026 calving events and sizes at Store Glacier in July 2017 using a terrestrial radar interferometer
- We find no single clear control on calving and clear variations in calving behaviour over time, producing a bimodal calving event-size distribution
- Our findings suggest that grouping glaciers by their dominant calving mechanism is not tenable, as this mechanism can change over time

This article has been accepted for publication and undergone full peer review but has not been through the copyediting, typesetting, pagination and proofreading process, which may lead to differences between this version and the [Version of Record](#). Please cite this article as doi: [10.1029/2020JF006051](https://doi.org/10.1029/2020JF006051).

This article is protected by copyright. All rights reserved.

Abstract

Calving and solid ice discharge into fjords account for approximately half of the annual net ice loss from the Greenland Ice Sheet, but these processes are rarely observed. To gain insights into the spatio-temporal nature of calving, we use a terrestrial radar interferometer to derive a three-week record of 8,026 calving events from Sermeq Kujalleq (Store Glacier, west Greenland), including the transition between a mélange-filled and ice-free fjord. We show that calving rates double across this transition and that the interferometer record is in good agreement with volumetric estimates of calving losses from contemporaneous UAV surveys. We report significant variations in calving activity over time, which obfuscate any simple power-law relationship. While there is a statistically significant relationship between surface melt and the number of calving events, no such relationship exists between surface melt and the volume of these events. Similarly, we find a 70% increase in the number of calving events in the presence of visible meltwater plumes, but only a 3% increase in calving volumes. While calving losses appear to have no clear single control, we find a bimodal distribution of iceberg sizes due to small blocks breaking off the subaerial part of the glacier front and large capsizing icebergs forming by full-thickness failure. Whereas previous work has hypothesised that tidewater glaciers can be grouped according to whether they calve predominantly by the former or latter mechanism, our observations indicate that calving here inherently comprises both, and that the dominant process can change over relatively short periods.

Plain Language Summary

We observe the release of icebergs by calving at a large glacier in Greenland for three weeks, during which we find 8,026 calving events across a wide range of environmental conditions. We show that our observation method (radar interferometry) agrees well with an independent method (aerial drone photography). We find that the type of calving varies significantly over time, but that there is no single mechanism that controls this variation; instead, it is due to multiple factors. This leads to two kinds of calving events: small blocks falling off the visible part of the front of the glacier, and large blocks of the entire thickness of the front (including the area underwater) breaking off. Previous work has assumed that glaciers can be grouped by which of these types of calving is more important, but we show that this is an over-simplification at large glaciers such as Store, as both these mechanisms are observed and both are the more important mechanism at different times.

1 Introduction

Tidewater outlet glaciers (i.e. glaciers that flow into the sea) drain 88% of the area of the Greenland ice sheet (GrIS) (Rignot & Mouginot, 2012). Ice discharge due to calving from these glaciers is currently responsible for 40% of GrIS annual net mass loss (equivalent to 0.33 mm a^{-1} global sea-level rise) (Mouginot et al., 2019). While increasing surface melt and runoff act to reduce the solid ice discharge due to the thinning it causes, tidewater glaciers are discharging more ice into the ocean (King et al., 2018). Therefore, understanding how calving occurs and its relationship to other processes in the tidewater-glacier system and external forcing becomes of central importance in forecasting the evolution of the GrIS in the coming decades and century.

Calving is an important glaciological process in tidewater environments in which glaciers discharge ice into fjords and coastal seas. It occurs when extensional stresses at the terminus produce fractures that intersect the calving front from either the surface or the base of the glacier

(Bassis and Jacobs, 2013; Benn et al., 2017b). Calving is governed by the distribution of stresses created by the flow of the glacier and its setting as well as environmental processes that can increase stresses at the terminus, such as buoyancy, surface melting or submarine melt undercutting (Benn et al., 2017b; Benn and Åström, 2018). As such, calving is a highly complex process that happens with little detectable warning based on small changes in one or more of the controlling variables (Åström et al., 2013; Benn et al., 2017a).

Calving at tidewater glaciers, due to this unpredictable nature, is therefore a difficult process to observe directly, meaning that obtaining information about overall rates or controls, which could allow the development of simple calving parameterisations, is challenging. Conventional remote-sensing does not offer sufficient temporal resolution, with satellites typically providing images a few days apart and even more recent techniques such as Unmanned Aerial Vehicles (UAVs) several hours apart (Chudley et al., 2019; Jouvet et al., 2017; van Dongen et al., 2019). Time-lapse cameras, whilst having sufficient temporal resolution, produce 2D imagery that is not easily converted into 3D volumes of calving events (How et al., 2018; Mallalieu et al., 2017; Vallot et al., 2019). Terrestrial laser scanning has been used (Pętllicki and Kinnard, 2016; Podgórski et al., 2018), but repeat surveys with this technique are problematic due to the large quantity of data in each survey, as well as the significant logistical effort required and the relatively short range of the instrument. Continuous and detailed datasets on calving behaviour at tidewater glaciers are thus lacking, yet understanding this process is crucial for advancing numerical models and for better prediction of tidewater-glacier behaviour and consequent sea-level rise. One possible solution to this issue is the use of terrestrial radar interferometry, which can provide high-resolution scans, both temporally and spatially, of a calving front (e.g. Voytenko et al., 2017; Walter et al., 2020). This novel method has so far only been applied to a limited number of tidewater outlets, but shows promise for providing the kind of continuous calving records that have been lacking in studies to date.

In this study, we use a real-aperture terrestrial radar interferometer (TRI) (Chapuis et al., 2010; Strozzi et al., 2012; van Dongen et al., 2019; Voytenko et al., 2017; Walter et al., 2020; Xie et al., 2019) to produce a directly observed, near-continuous, 3-week record of calving events for a major Greenlandic outlet glacier. The high resolution of this technique, both spatially and temporally, allows us to characterise 8,026 calving events in terms of size and frequency, while exploring the effect of different environmental factors.

2 Methods

2.1. Study site

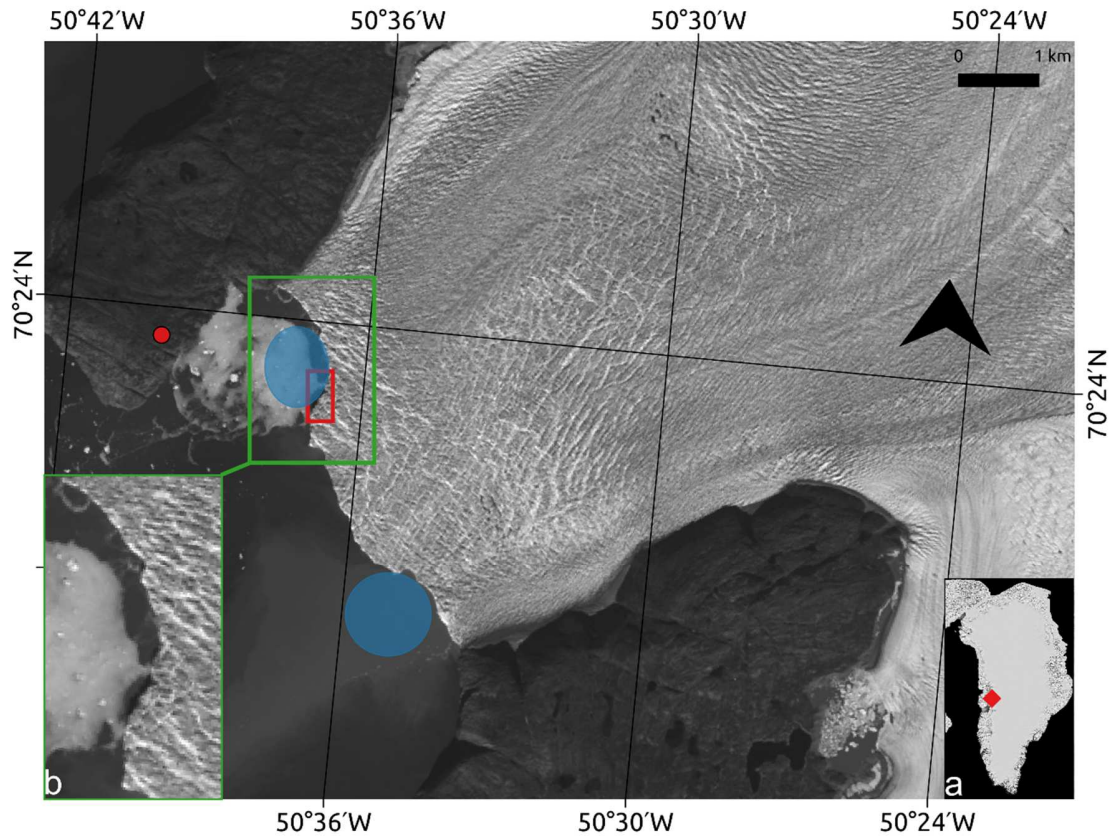


Figure 1 – Location of Store Glacier (inset **a**) and location of TRI and time-lapse camera (red circle). The study area is outlined in green (inset **b**). The red rectangle represents the area zoomed in on in Figures 2 and 3 and the blue circles show the two regions where surfacing plumes are commonly observed in the time-lapse imagery. Background image from Landsat 8, acquired on 10th October, 2016.

Sermeq Kujalleq (Store Glacier) (70.4° N 50.6° W, Figure 1), referred to here as Store, is one of the largest tidewater outlet glaciers on the west coast of Greenland. The glacier discharges around 12 Gt annually into Ikerasak Fjord (Rignot et al., 2016) in the southern end of Uummannaq Bay. The calving front of Store is 5 km wide, with surface velocities reaching up to 6600 m a^{-1} (Joughin, 2018), and is located at a lateral constriction in the fjord on top of a basal pinning point, making the terminus position relatively stable (Todd et al., 2019) with no observed retreat since at least 1985 (Catania et al., 2018). This stability makes it an ideal target for developing calving models (e.g. Morlighem et al., 2016; Todd et al., 2018; Todd and Christoffersen, 2014; Xu et al., 2013) and for observing tidewater-glacier processes in a ‘natural’, i.e. unperturbed setting. However, behind this pinning point, Store sits in a deep trough that could condition it for rapid retreat should the front be pushed back from the pinning point

(Aschwanden et al., 2019). This means Store is additionally interesting, as it may provide information on the transition from a stable calving front to a retreating calving front in the future.

2.2. Radar set-up

The TRI used in this study was a Gamma Remote Sensing Ground-based Portable Radar Interferometer II (GPRI-II). This is a Ku-band ($\lambda=1.75$ cm), real-aperture, rotating instrument that has a range of up to 16 km with a range resolution of 0.75 m and an azimuthal resolution proportional to slant range with a ratio of 8:1000 (i.e., an azimuthal resolution of 8 m at 1 km distance) (Werner et al., 2008). The instrument has one transmit and two receive antenna, spaced 25 cm apart, allowing measurement of spatio-temporal change in calving-front dynamics. Topography can be computed by comparing images from both antennae taken at the same time.

The GPRI-II was located about 2 km from the glacier terminus on the northern side of the fjord, on a rocky promontory overlooking the calving front (Figure 2). A Canon EOS 750D time-lapse camera was also installed next to it. The TRI was set to scan at a repeat interval of 3 minutes continuously for 21 days (each scan lasted approximately 30 s), between 18:25 on the 5th and 11:01 on the 26th July 2017.



Figure 2 – Photo showing set-up of the TRI overlooking the calving front of Store.

2.3. Radar data processing

We used the interferogram record from the TRI, processed using the Gamma software suite, to generate a sequence of digital elevation models (DEMs) from which a record of calving events at Store could be extracted. Topography can be computed from the difference in path lengths between the transmitting and receiving antennas, which is related to the measured interferometric phase and wavelength of the radar. In this case, the topography was calculated following the method of Strozzi et al. (2012), with the resulting DEMs being resampled to a 10 m by 10 m resolution and reprojected to Cartesian co-ordinates. As the measurements from each antenna are simultaneous, no atmospheric or phase displacement corrections are needed (Strozzi et al., 2012). Inspection of the resulting record revealed a small number of significant phase breaks and changes in orientation of the TRI over the course of the observation period, which we ascribe to periods of high winds buffeting the instrument. We identified four stable periods, covering the majority of the three-week record (18 out of 21 days), within which orientation and instrument biases were constant. Rotations were applied to each period to ensure alignment of DEMs, as set

out in Table 1. These rotations were calculated manually by comparing the position of the fjord walls with reference satellite imagery.

Table 1 – Stable periods and applied rotations to ensure alignment. Times are in local Greenland time WGST).

Name	Start	End	Rotation
Period 1	18:25 05/07/17	07:18 14/07/17	0
Period 2	19:06 14/07/17	23:36 18/07/17	-10°
Period 3	14:06 21/07/17	01:03 26/07/17	-3°
Period 4	01:09 26/07/17	11:01 27/07/17	0

To identify calving events, we difference consecutive DEMs produced at each timestep within the above periods (Table 1). Initially, we spatially interpolated the DEMs to fill gaps, but this created substantial interpolation artefacts in areas of radar shadow and poor radar return. We therefore avoid interpolation and restrict our analysis to the northern embayment of the calving front (inset **b.** in Figure 1), as the southern embayment was frequently obstructed through the study period by the protruding terminus of Store Glacier, and did not generate good-quality radar returns. This decision means some calving events may be split into several smaller events by no-data pixels, but means that we avoid false positive events. Where DEMs showed anomalous differences (tens of metres of change or more in mean pixel value across the entire DEM) in elevation values, they were deleted from the record before differencing was undertaken, to leave a consistent set of DEMs within each of the periods identified in Table 1.

Although no ground control was reliably available within the viewing angle, we have confidence in the data as the remaining DEMs, when considered consecutively, do not show decorrelation within each period. Relative height changes can thus be reliably measured, which is sufficient for our purpose, so we did not pursue a solution to this issue. We did not perform additional correction for differences in atmospheric conditions between DEMs as noise created by this will have been filtered out by the steps detailed below, and accounted for within the error estimate described in Section 3.

To identify calving events, the remaining DEMs were then differenced within each period, though no differencing was undertaken across different periods. Calving events were then extracted. To ensure elevation changes caused by serac collapse inland on the glacier, or by iceberg movement or fragmentation in the fjord, were ignored, a mask of the ice-front position for each period was produced by manual digitisation, leaving the area around the calving front (a few hundred metres in either direction), where calving events would be detected, unmasked. The exact position of the calving front within the unmasked area for each DEM was then digitised using an edge-detecting Sobel filter. Valid calving events were identified as negative changes in elevation of more than 10 m with at least one pixel on the digitised calving front and entirely within the unmasked area. Additionally, events of 3 pixels or fewer in area (i.e. 300 m² in area or less) were filtered out. The area of each event was then calculated by summing up the number of contiguous DEM pixels meeting the above criteria. Our approach is similar to Walter et al. (2020), although we use a slightly wider frontal mask because Store is larger and more dynamic. We also use a smaller number of pixels as a threshold for determining real calving events compared to noise, as our pixel size is larger, but the required adjacent area (>300 m²) is the same.

Accepted Article

Finally, the volume of each event was calculated by multiplying the area of each pixel by the elevation change, producing a record of subaerial calving volumes and frequencies for the northern half of Store's terminus. This method therefore imposes a minimum detectable calving event size of 4000 m³ (i.e. 4 pixels of area (10 x 10 m² each) x 10 m of elevation change), so smaller events are not part of the analysis in this paper. This minimum detectable size is also comfortably in excess of our estimated error (see Section 3), giving us confidence that we are measuring actual calving rather than noise. To support the time-series data, we compare it to total daily surface melt from the Store drainage basin from modelled RACMO 2.3p2 data (van Wessem et al., 2018) at 1 km resolution. We also manually examine the TRI footage to determine when the majority of the northern side of the calving front and fjord were mélange-covered and when at least one plume was visible in the area. Counts and volumes of calving events during ice-covered and ice-free periods, and of plume-visible and plume-absent periods, were subsequently standardised to enable direct comparison. We express the calving events as expected totals for an 'average' day by working out how many calving events in the TRI record fall within the ice-covered/ice-free and plume-present/plume-absent periods and scaling these totals to a period of 24 hours. We of course recognise these binary categorisations are simplifications of complex processes; we use them for analytical convenience.

3 UAV and time-lapse data

For comparison and validation, we combine TRI data from Store with DEMs produced photogrammetrically with a 20 cm resolution from contemporaneous UAV surveys. Overlapping imagery was captured using a Sony α6000 camera mounted on a Skywalker X8 2m fixed-wing UAV. Flights were flown at an altitude of approximately 450 m above the glacier surface., targeting a ground sampling distance of ≈11 cm, a forward overlap of 80%, and a sidelap of 60%. 3D models were produced using Structure-from-Motion with Multi-View Stereo (SfM-MVS) photogrammetry using Agisoft Metashape software. Models were geolocated via aerial triangulation using a L1 carrier-phase GPS receiver mounted on the UAV, post-processed kinematically against a bedrock-mounted GPS base station. For a full outline of the methods, see Chudley et al. (2019). We use DEMs produced from flights over the calving front at 2017-07-12 at 22:00 and 2017-07-13 at 10:00 WGST. Calving volumes were calculated by differencing the two DEMs, manually delineating the calved area and then multiplying the area of each pixel by the elevation change. To correct for ice flow between the two UAV flights, we perform this volume calculation with the DEMs "as is" (i.e. implicitly assuming that all calving happened just before the second UAV flight) to derive a minimum volume. We then perform the same calculation, but with the later UAV DEM georeferenced to the earlier one using identifiable features on both DEMs as ground control points (i.e. assuming that all calving happened just after the first flight) to obtain a maximum volume. We then calculate the difference between these two volume estimates, divide it by two (as the TRI data show the volume of calving was spread nearly time-symmetrically about the mid-point between the two UAV flights) and subtract the result from the maximum estimate to obtain our final figure presented below.

We also use the contemporaneous UAV observations to assess the error bar on the TRI observations. The error on the UAV-derived DEMs has been shown to be around 10 cm in both the horizontal and vertical directions (Chudley et al., 2019), which means we can reasonably use these as the ‘true’ surfaces when we compare against the much coarser TRI DEMs. We georeferenced the TRI observations from 18:18 on the 12th July and resampled the contemporaneous UAV DEM to match. We then differenced the TRI DEM and the resampled UAV DEM to estimate the error bar (1σ) in the TRI data. After removing no-data pixels and those more than three times the interquartile range above the third quartile or below the first quartile, we find an error bar of 5.4 m for the TRI observations compared to the UAV observations. This validates our choice of the 10 m threshold, as described above, for discriminating between ‘real’ calving events and noise, and also our discarding of any DEMs that showed jumps in mean elevation values of tens of metres. This error bar means the maximum error on volume measurements is therefore 540 m³ per pixel (5.4 x 10 x 10) or at least 2160 m³ per event (4 pixels minimum), which is a) well below our minimum threshold of detectability imposed by the processing method described above (4000 m³), giving us confidence that our results represent actual calving, rather than noise, and b) is sufficiently small that it does not materially impact the presentation of our results.

In addition, we used stationary time-lapse images taken at 5-minute intervals by a camera installed next to the TRI throughout the field season, including the 12-hour period separating the two UAV surveys. These images are used here purely as a visual record.

4 Results

4.1. Comparison of TRI with UAV and time-lapse data

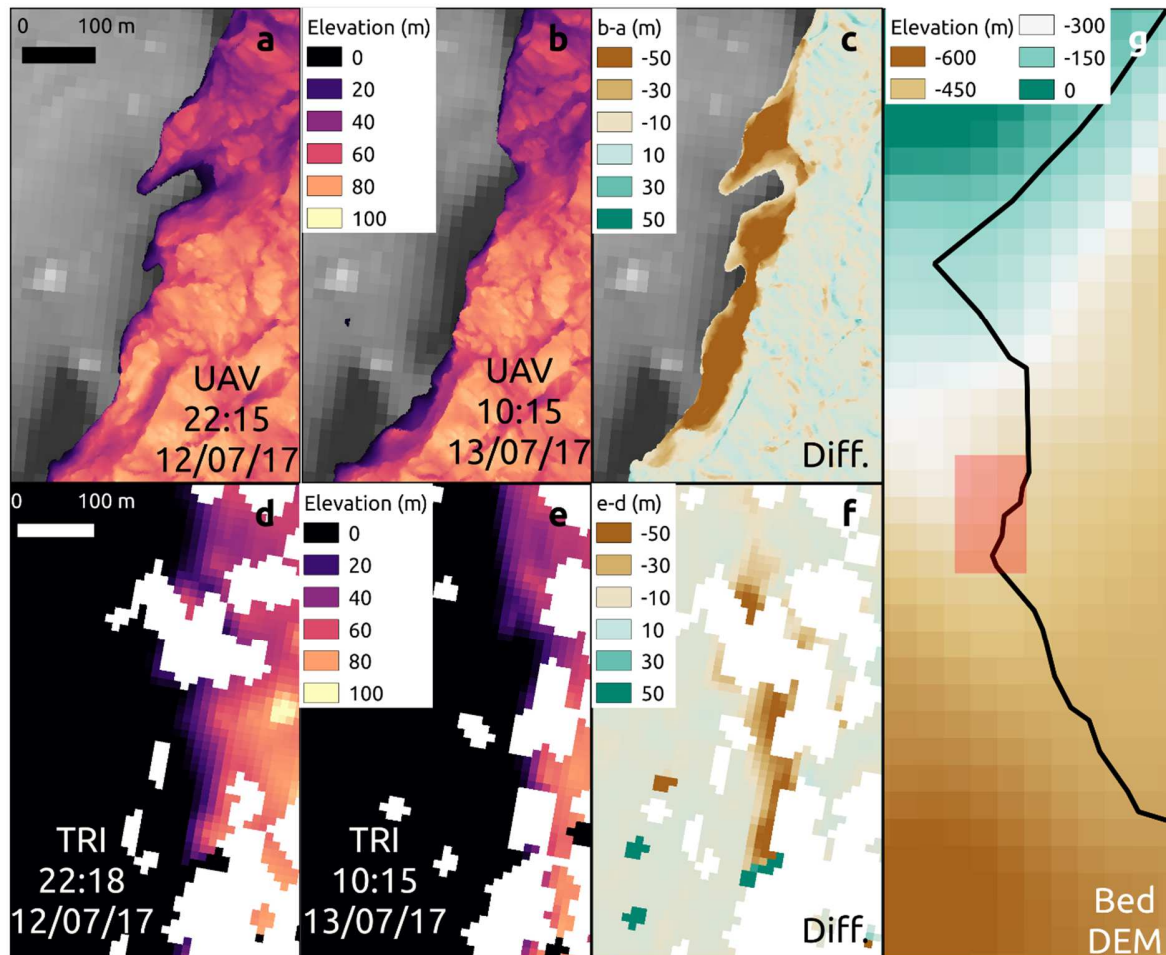


Figure 3 – Comparison of calving loss detection across UAV and TRI datasets. Panels **a** and **b** show a large-scale calving loss from UAV-derived DEMs acquired across a 12-hour period; panel **c** shows the difference between panels **a** and **b**. Panels **d** and **e** show the same calving loss on TRI-derived DEMs; panel **f** shows the difference between panels **d** and **e**. Panel **g** shows the location of the calving at the front of Store (red box) and the bed DEM (see Cook et al. (2020)) used in volume calculations. The black line is the approximate outline of the calving front and northern lateral margin of Store. White areas represent line-of-sight radar shadows due to poor radar coherence or surface topography; see Section 5.3 for discussion of these data gaps.

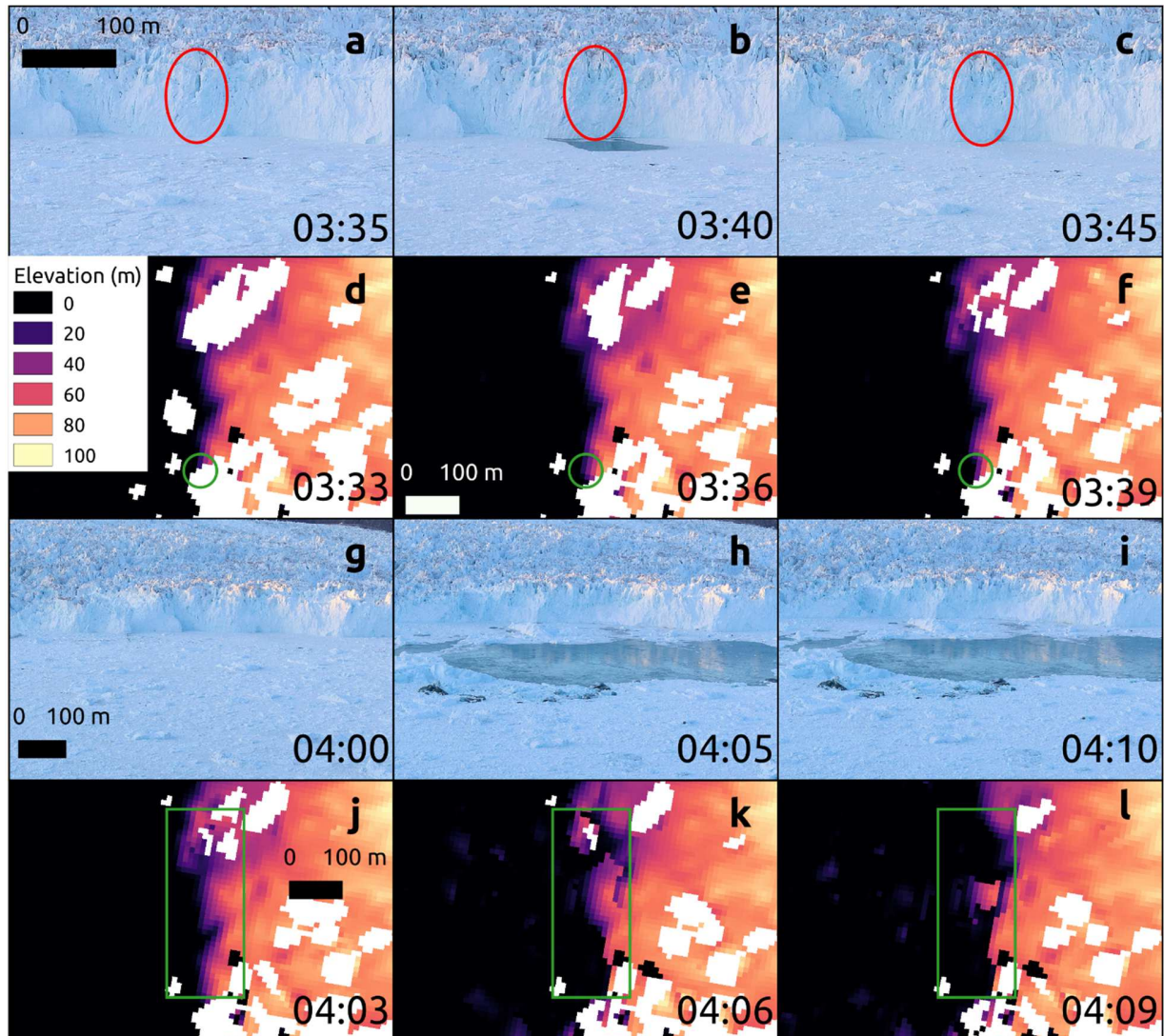


Figure 4 – Comparison of specific calving-event detection across time-lapse and TRI datasets. Panels **a-c** show a smaller constituent calving event of the total loss in Figure 3 from time-lapse imagery (event marked by red ellipse); Panels **d-f** show the same event from the TRI's perspective (event denoted by green circle). Panels **g-i** show the largest constituent calving event of the loss in Figure 3 from time-lapse footage; Panels **j-l** show this event from the TRI's viewpoint (inside green box). See Section 5.3 for discussion of the data gaps.

Before extracting the full TRI record of calving events, we compare the TRI observations against two contemporaneous high-precision DEMs from UAV surveys separated by 12 hours. We also use time-lapse camera images captured sequentially at 5 minute intervals during this period (Figure 3), focusing specifically on the section of the calving front denoted by the red box in Figure 1. The UAV-derived DEMs (Figure 3a-c) show a distinct change in the terminus position, but cannot specify whether calving occurred as a single large event or multiple smaller events for the total $\approx 1,400,000 \text{ m}^3$ in subaerial volume loss calculated by differencing the two DEMs. This is resolved by the TRI, which captured identical frontal positions (Figure 3d-f) and how terminus geometry changed (Figure 4). With data acquired every 3 minutes, the TRI record reveals a total

of 48 individual calving events over the 12-hour period between the two UAV surveys. Figures 4a-c and 4d-f show one of the smaller constituent events, from the perspective of the camera and TRI, respectively, and Figures 4g-i and 4j-l show the largest constituent event, which generated about 40% of the total subaerial volume loss detected over the 12-hour period. As can be seen, the time-lapse and TRI footage both agree on the timing of the calving events. Only 6 out of the observed 48 events (12.5%) exceeded a size of $5 \times 10^4 \text{ m}^3$ (Figure 5), but these larger events were responsible for 56% of the volume loss across the 12-hour period. The smaller events, whilst seven times more numerous, contributed just under half (44%) of the volume of ice calved.

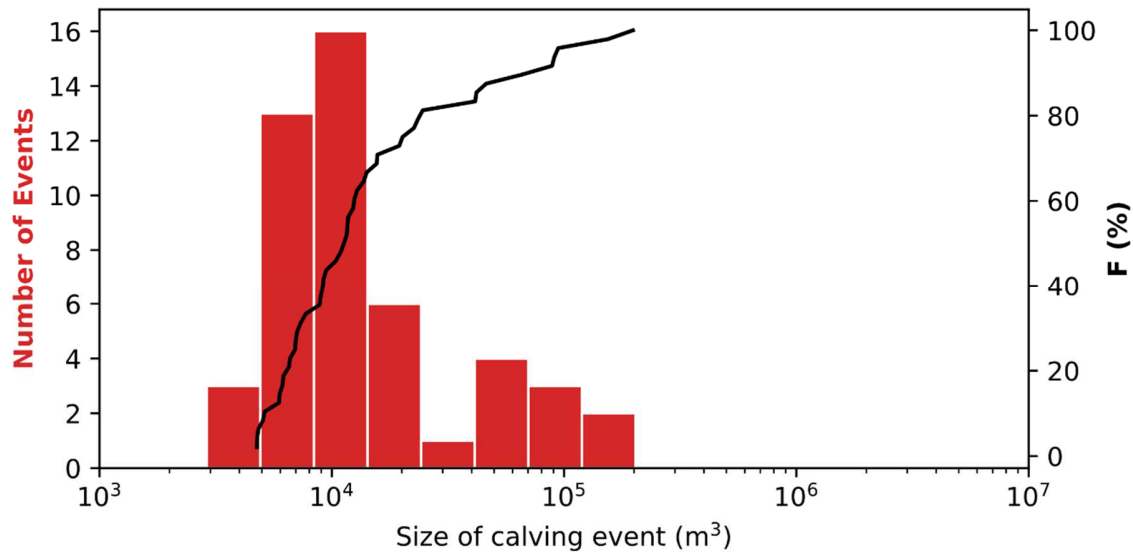


Figure 5 – Cumulative distribution function (right axis) and histogram (left axis) of frequency-magnitude relationship of single set of calving events at Store for the 12 hours from 22:17 12/07/17 to 10:15 13/07/17 considered in the UAV validation exercise. Compare with Figure 6 below. Size refers to the observed subaerial volume.

The total subaerial ice volume loss detected by differencing the two UAV DEMs is $1,404,000 \text{ m}^3$. When we sum up all the events within the same area detected by the TRI we obtain a total subaerial ice volume loss of $1,240,000 \text{ m}^3$, which is a discrepancy of only 12% compared to the independent UAV method. Assuming that the calving front remains close to vertical, and using the bed DEM shown in Figure 3g, we estimate that the accompanying submarine volume loss is $11,900,000 \text{ m}^3$, giving a total calving volume of $13,150,000 \text{ m}^3$. Given that the submarine loss is ≈ 9 times the subaerial loss derived from the UAV and TRI DEMs, the setting of the glacier is close to floatation. This 12% mismatch figure between the TRI and the UAV data also provides a useful constraint on calving under-estimation from the TRI due to radar shadows.

4.2. Calving magnitude-frequency distribution

Over the entire three-week period of observation, we find a total of 8,026 calving events with a mean size of $48,428 \text{ m}^3$ (Figure 6). Two thirds of the events by frequency are under $50,000 \text{ m}^3$ in subaerial volume, but these only account for 15% of the total volume loss, excluding the small events below the detection threshold. Very large events, over $500,000 \text{ m}^3$ in subaerial volume, are much rarer, totalling only 35 in the record, or 0.4% of total events, but are responsible for a

disproportionate 8% of total volume loss. The events in-between ($50,000\text{-}500,000\text{ m}^3$) are consequently responsible for the vast majority of total volume loss, at 77% (Figure 6).

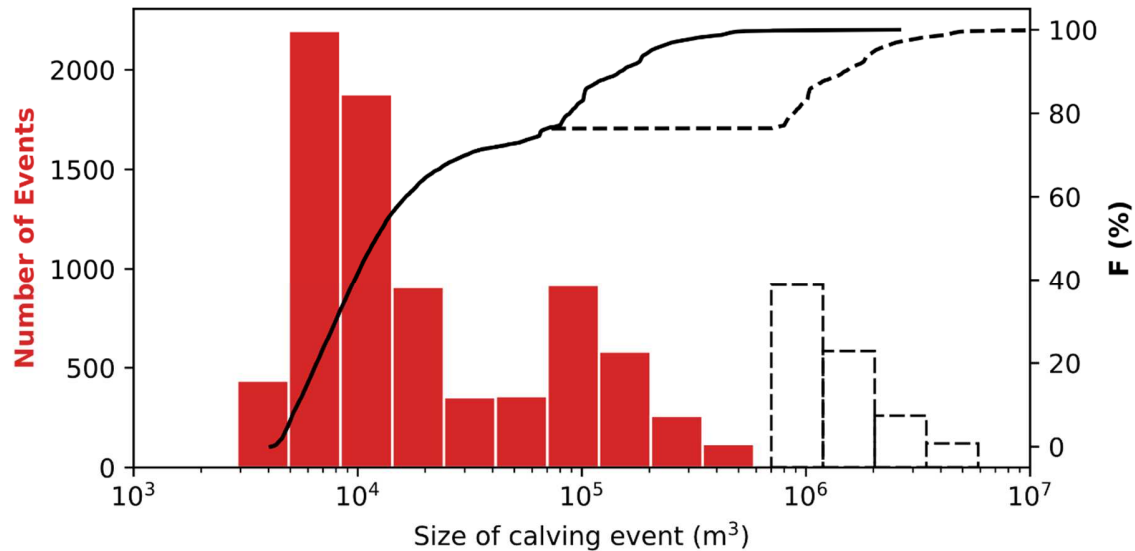


Figure 6 – Cumulative distribution function (right axis) and histogram (left axis) showing size-frequency relationship of all detected calving events observed subaerially at Store for 23 days from 5th July to 27th July 2017. Dashed black bars show posited actual size of full-thickness calving events which is estimated to be 9 times greater than the subaerially observed fraction because the glacier is near floatation. Dashed black line shows the cumulative distribution function based on the inferred actual size (dashed bars) rather than the observed red bars ($>7 \times 10^4\text{ m}^3$). Compare with Figure 5 above.

4.3. Time-varying behaviour in calving

Considering the distribution of calving events over time (Figure 7), we observe low calving activity of <200 events per day prior to 8 July when the fjord was still frozen and filled with mélangé. On the 8th, when the mélangé broke up, calving activity immediately increased to 300 events, mostly driven by an increase in larger ($>10^5\text{ m}^3$) icebergs. From the 9th to the 14th, calving activity increases further, to ≈ 400 events per day, with a continued high proportion of larger events. From the 15th to the 17th, calving activity declines back to ≈ 300 events per day, with a particular reduction in the number of the largest ($>10^6\text{ m}^3$) category of events, before starting to increase again, on the 18th, with a doubling in the number of the smallest ($10^3\text{-}10^4\text{ m}^3$) events. Due to weather interference (high winds buffeting the TRI), there is a data gap on the 19th and 20th. However, immediately after this gap, the 10 hours of data collected on the 21st show a day of significant calving activity (Figure 7). Calving volumes peak with a value of nearly $2,000,000\text{ m}^3$ on the 22nd while the daily number of events peaks on the 24th at 721, or 30 events per hour. In general, the number and volume of calving events remain high between the 18th and 24th, though volumes are lower from the 23rd onwards.

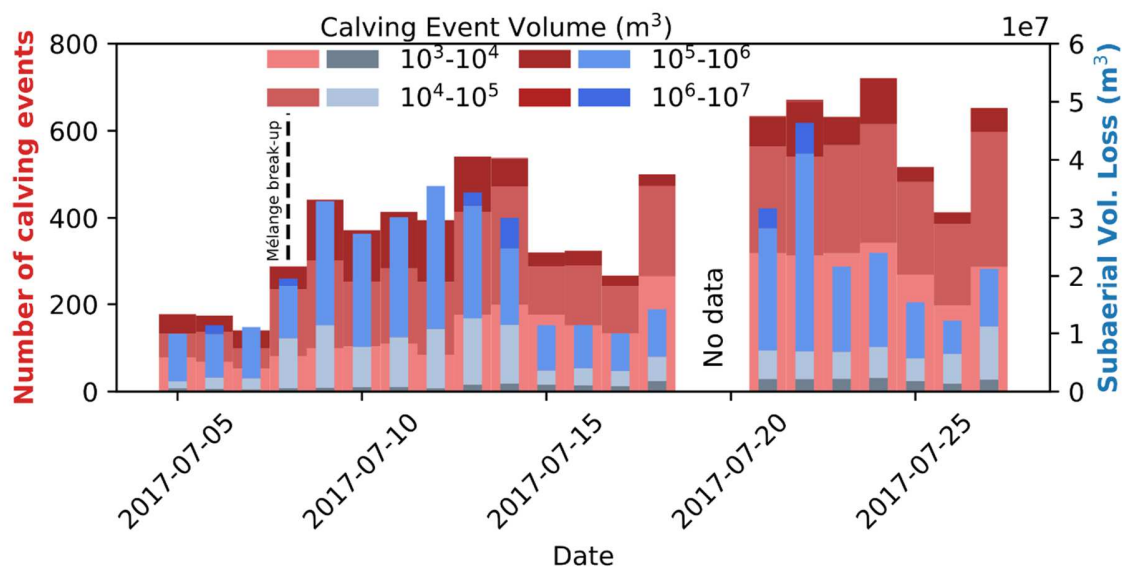


Figure 7 – Time series of calving events at Store. Bars stacked by volume of event. Daily counts are shown by thick red bars; cumulative volumes by the inner blue bars. Note how calving activity increases on the 8th July when the proglacial mélange broke up.

A possible trigger for calving activity is the weather or, more specifically, surface melt variations due to changes in air temperature, as greater surface melt is hypothesised to enhance the depth of surface crevasse penetration (Benn & Åström, 2018). We examine this by plotting calving counts and volumes (Figure 8) against surface melt for the Store basin, derived by integrating surface runoff from the RACMO dataset across the Store basin. Ignoring days with incomplete or no calving data, we find correlation coefficients of 0.42 for the counts, which is significant at the 95% confidence interval ($p < 0.05$), but only 0.12 for the volumes, which is statistically insignificant.

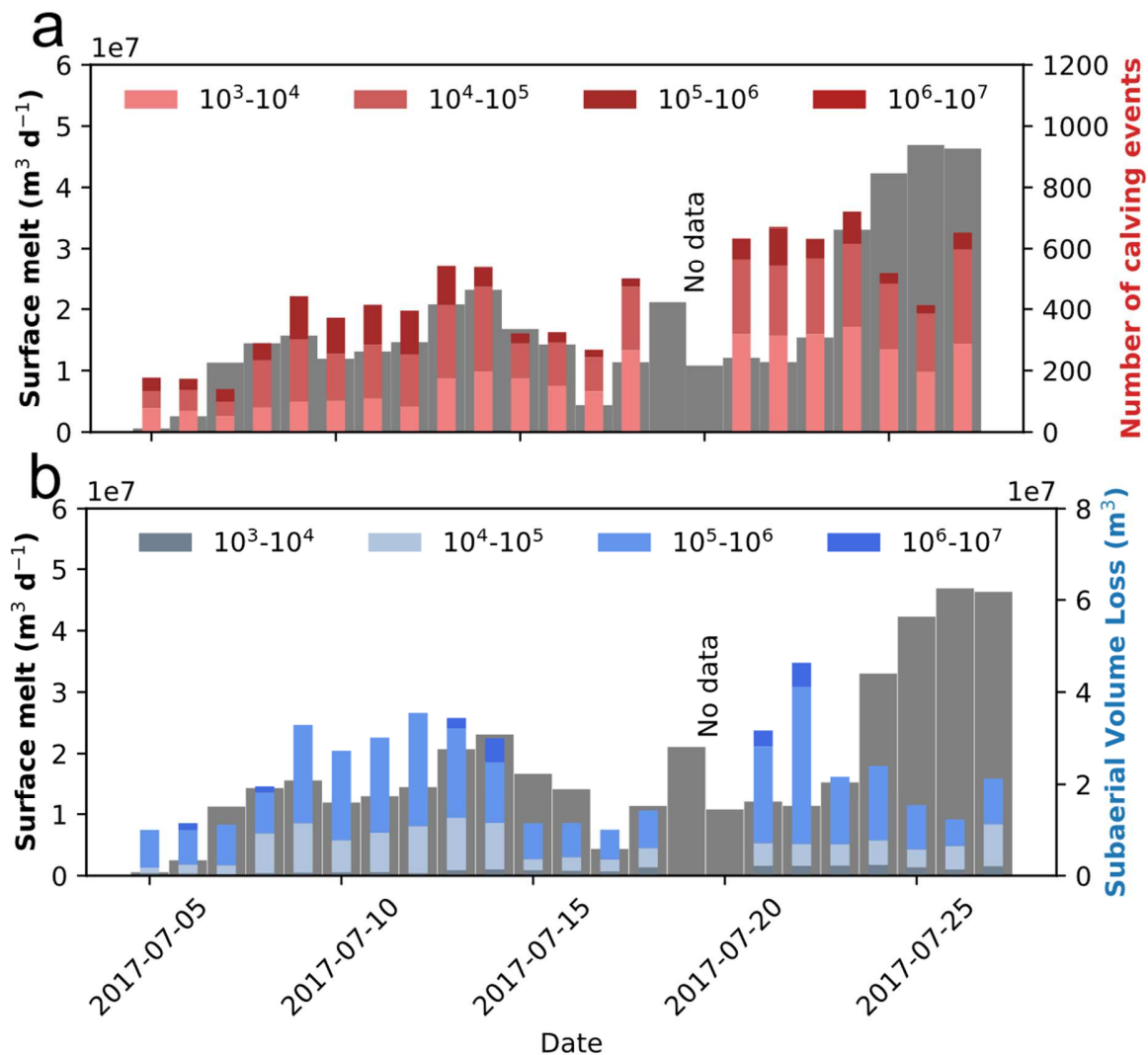


Figure 8 – Time series of surface melt from RACMO 2.3p2 data (grey bars, left axis) and TRI-derived calving events (coloured bars, right axis). **a** calving event frequency (red bars) and **b** calving volumes (blue bars).

To examine any diurnal variation in calving activity, we investigated the hourly record of calving on specific days (Figure 9), each taken from one period of calving activity: the 6th, for the pre-mélange-break-up state of calving; the 11th, in the period of sustained higher calving following break-up; the 15th, in the following period of lower calving; and the 23rd, for the second period of higher calving.

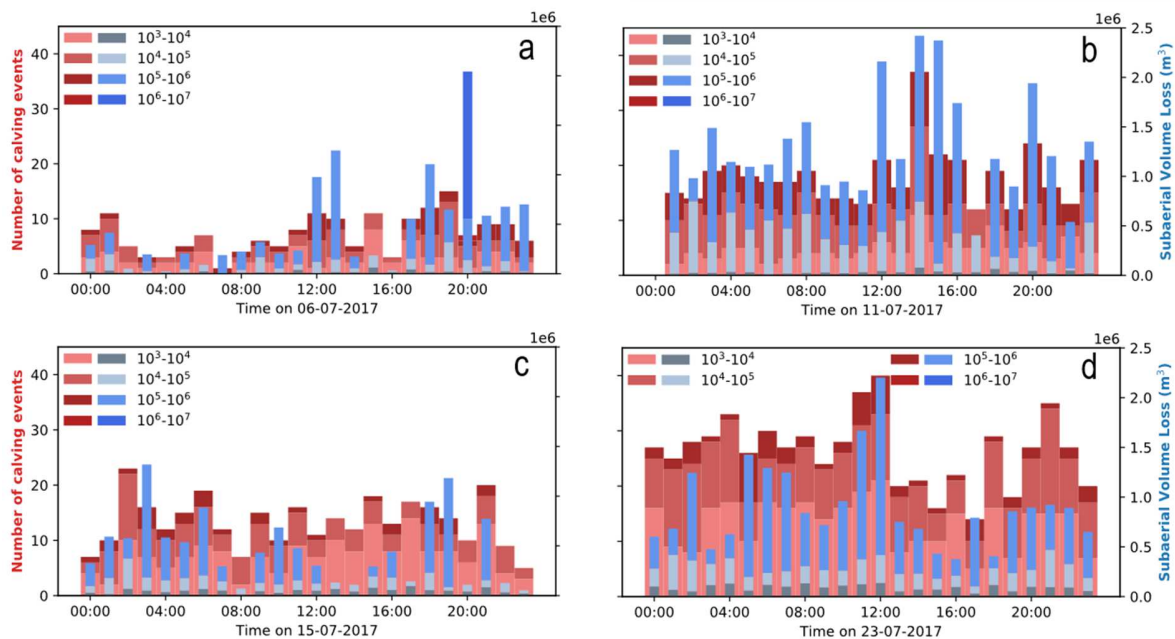


Figure 9 – Time series of calving binned by hour from **a** 06/07/2017 (before mélangé breaks up), **b** 11/07/2017 (high calving activity following mélangé break-up), **c** 15/07/2017 (reduced calving activity), and **d** 23/07/2017 (renewed high calving activity).

As Figure 9 shows, there are significant intra-day variations but no statistically significant diurnal trend in calving activity. However, there are shared features across all four days seen as nominal peaks in counts and volumes around $04:00 \pm 2$ hours; $12:00 \pm 2$ hours and $20:00 \pm 2$ hours WGST. The most noticeable recurring peak is the one at midday, although inspection of all seventeen days with sufficient data to perform the diurnal analysis shows it is not a persistent feature and occurred only on five days (including the 6th, 11th and 23rd, shown in Figure 9). We also investigated whether a link between the tidal cycle and calving activity could be discerned, but found no statistically significant relationship.

4.4. Spatiotemporal variations in calving

Two major factors that are hypothesised to influence calving rates are the presence/absence of mélangé in the fjord and of active meltwater plumes fed by subglacial discharge. We assess the impact of both of these at Store by comparing calving counts and volumes for periods of mélangé presence and absence and of visible plume presence and absence within the study area (Figure 10). In both cases, the counts and volumes are expressed as an average rate per day. We observe more than a doubling in the number of calving events in the absence of mélangé (from 271 events per day with mélangé to 588 events without), compared to when it is present, and a concomitant 44% increase in volumes. In the presence of visible plumes, the number of calving events increases by 70%, from 395 per day to 672, but the volume loss from these events only increases very slightly, by 3%, compared to when no plumes are visible.

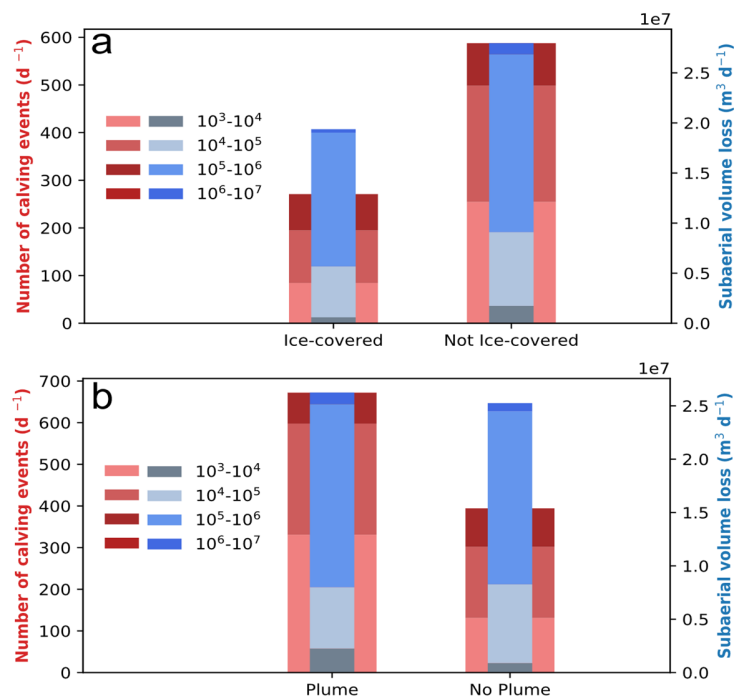


Figure 10 – Calving event counts and volumes during times when **a** mélangé is present compared to when it is not, and **b** when plumes are visible compared to when they are not. Note how mélangé presence suppresses calving activity and how plume presence increases the frequency of smaller and mid-sized calving events.

5 Discussion

5.1. Calving behaviour

The observed magnitude-frequency distribution of calving shows a positively skewed relationship (Figure 6): there are far more smaller events than larger ones, though the rarer larger events account for most of the volume loss. The smaller events mostly represent occurrences similar in style to that shown in Figure 4a-f, i.e. detachment of relatively small blocks of ice from the subaerial portion of the calving front that then fall into the fjord. The larger events are instead exemplified by Figure 4g-l, where entire sections of the front peel off and topple over. No large tabular-style calving events are observed here; at Store, these events usually happen on the floating southern part of the calving front and not on the grounded northern section analysed here (Todd et al., 2018). Contrary to other observations (Åström et al., 2014; Chapuis and Tetzlaff, 2014; Walter et al., 2020), the calving events discussed here do not follow a clear power-law distribution (Figure 6), with the cumulative distribution across the entire dataset suggesting a bimodal sequence of calving events (Figure 11). One peak is at a magnitude of the order of 10⁴ m³, with another on the order of 10⁵ m³. We hypothesise that the first peak represents the smaller calving events described above, where only a (relatively) small subaerial portion of the calving front calves. The second peak then represents the larger calving events in which a larger portion of the front breaks off. We explain the bimodal event size distribution (with a paucity of intermediate sized events) to be due to the mechanics of fracture propagation: if a fracture reaches the waterline, it will usually fill with water, which will propagate it deeper, which will further increase the water pressure in a positive feedback. It is also possible that surface fractures

will intersect basal crevasses that propagate upwards from the base (Todd et al., 2018). Both of these mechanisms can generate large, full-thickness calving events. The first peak consequently represents those events where the initiating fracture does not reach the waterline, limiting calving to detachment of blocks on the subaerial region of the calving front; the second peak represents those where the fracture has reached the waterline and continued to the base, or intersected a basal crevasse, resulting in events that are an order of magnitude greater or even larger. Because our observations are limited to the subaerial portion of the front and we know the terminus is close to floatation, the larger events reported with a modal peak of 10^5 m^3 may be the subaerial portion of events with a true modal size closer to 10^6 m^3 (as shown by dashed black lines in Figure 6). As such, intermediate events are rare, because detachment of blocks can only be so large (i.e. a few tens of metres of ice thickness across a small section of the front) whereas the large toppling of bergs can only be so small (i.e. hundreds of metres of ice thickness across a larger portion of front).

Returning to how previous calving datasets have shown a power-law distribution for the magnitude-frequency of events, we hypothesise that this is primarily due to the relatively short duration of previous observations (typically a week or less – 4 days for Chapuis and Tetzlaff (2014); 6.5 days for Walter et al. (2020)). The bimodality we observe here is a result of two characteristic iceberg size distributions: one being small blocks of ice falling off the front due to instability from fractures that are tens of metres deep and the other being larger bergs forming when fractures penetrate the whole ice-column. Superimposed on this bimodality is a time-varying calving behaviour (Figure 11). In the days leading up to mélange break up on the 8th, this bimodality is evident in a similar pattern to that found for the whole dataset. Thereafter, from the 8th through to the 13th, there is a higher-than-average representation of the larger class of calving events while the smaller class is under-represented, before the 14th returns to near the overall distribution. After the 14th, however, the rest of the dataset tends towards a relative under-representation of the larger events, while the smaller events are more frequent than average. Therefore, if our observations had been limited to a few days only, e.g. as shown in Figure 5, we might have concluded that a power law fitted on the slope of the cumulative distribution function would be an accurate representation of the data; yet this slope varies greatly over the period of observations (Figure 11). We therefore suggest that, to get an accurate picture of the calving distribution at a tidewater glacier, detailed observations of calving need to be maintained for at least a week, ideally for a fortnight or even longer. Shorter observational periods run the risk of missing out on aspects or distinct periods of calving behaviour or of attempting to fit a single power law to a distribution that might have multiple distinct causes, each best-represented by a single power law. In the case presented here, a separate power law, based on the variety of cumulative distribution functions we observe (Figure 11), would be needed for a) the system before mélange break-up (5th-7th), b) the system in the immediate aftermath of mélange break-up (8th-14th), and c) the system in the later post-break-up period (15th-27th) (Figure 8, Figure 11). Doing so, we find best-fit power laws with exponents of 0.53, 0.64 and 0.57, respectively, and R^2 values of 0.58, 0.73, and 0.44, respectively, suggesting that this calving dataset is mostly poorly represented by power laws, with the possible exception of the immediate post-mélange-break-up period, though, even in this period, we still observe pronounced bimodality.

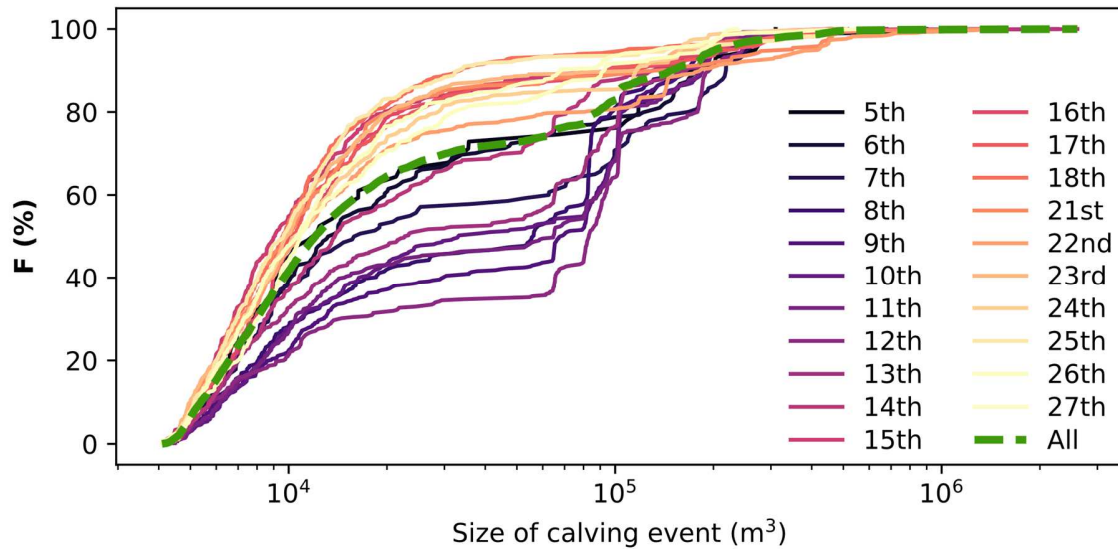


Figure 11 – Cumulative distribution function for calving events observed from 5th July to 27th July 2017, with coloured lines denoting distribution on specific days and dashed green line showing the overall distribution. Notice how days earlier in the observation period cluster below the overall average distribution, whereas those later in the period cluster above it.

5.2. Calving controls

The TRI record from Store provides some interesting information on the global distribution and controls on calving. We find a sustained 6-day period of higher calving activity in the aftermath of *mélange* break-up on the 8th July (Figure 7), with rates more than doubling compared to before break-up. Previous modelling work on Store (Todd et al., 2018) suggests this corresponds to the loss of backstress from the *mélange*, which provides a resisting force when the *mélange* is rigid. When the backstress is lost, this force disappears, facilitating crevasse propagation of sufficient depth to trigger detachment of full-thickness sections of the front (Amundson & Truffer, 2010). As such, we find the highest proportions of the largest events at this time, with the largest two categories of events ($>10^5$ m³ in terms of subaerial volume and potentially $>10^6$ m³ in total volume) making up an average of 33% of all events between the 9th and the 12th, inclusive, compared to an average of 24% beforehand and 11% afterwards. We then see a period of renewed calving intensity from at least the 21st to the 24th, this time predicated on smaller events, which seems to tail off on the 25th and 26th before possibly starting to pick up again on the 27th, the very last day of the record. An interesting perspective on this behaviour is provided by the theory of calving fronts as self-organised critical systems (Åström et al., 2014; Chapuis & Tetzlaff, 2014), whereby the front continually oscillates around a critical point that is determined by the environmental boundary conditions – air and water temperature, bed topography, glacier geometry, etc. Fronts that are subcritical will tend to move towards the critical point, building up instabilities and manifesting small-scale, subdued calving behaviour. At some point, the calving front will find itself in a state of supercriticality due to a change in the environment or as it overshoots the critical point, which produces large-scale, sustained calving as the system adjusts back towards the critical point. Therefore, removal of the *mélange* can be interpreted as shifting the critical point of the system, suddenly placing the calving front of Store in a position of

overshoot, and therefore supercriticality, manifested through a series of large calving events (the initial period of strong calving from the 8th-13th). The now-subcritical system then steadily re-advances towards the critical point, building up instabilities as it does so, and exhibiting small calving events (the quieter period of calving from the 14th to the 18th). Although greater calving activity is observed subsequent to this until the end of the record (the 19th to the 27th), the shape of the cumulative distribution functions (Figure 11), with a marked dominance of smaller events, suggests this is a prolongation of the subcritical phase, rather than a return to supercriticality.

This theory also helps to explain the very poor correlation found between calving event size and amount of surface melt (Figure 8). Whilst there is statistically significant correlation between surface melt and the *number* of calving events (Figure 8a), there is none between surface melt and the *volume* of events (Figure 8b). Increased surface melt should enhance fracture propagation by increasing the amount of water available for hydrofracturing at the surface, or by generating more vigorous freshwater-plume circulation at the front, leading to increased submarine melting and undercutting (O'Leary & Christoffersen, 2013) – this link is discussed further, below. Hence we would expect to find a link between surface melt and counts of calving events. Whether these fractures grow in such a way as to produce large or small calving events, however, would seem to be primarily determined by other factors, such as whether the system is in a subcritical or supercritical state.

A link between surface melt and calving activity is also observed (Figure 8), but this does not translate into the consistent appearance of a midday peak in calving that could be driven by increased insolation and therefore surface melt, thus driving fracture propagation, at this time of day. This reinforces the conclusion that surface melt may influence calving on some days but not all days, and only insofar as sufficient water becomes available over multiple days to drive hydrofracture. However, this mechanism is not a primary driver of calving activity..

We also examine two important factors contributing to the criticality of the system (Figure 10). In accordance with the pattern of activity observed in Figure 7, we find much stronger calving activity in the absence of *mélange* compared to when it is present (Figure 10a; compare Figure 7). One point worth noticing is that the largest of two observed modal peaks in calving accounts for a greater proportion (28%, representing 888 events) of the total calving count when *mélange* is present compared to when it is not (15%, representing 1041 events), suggesting that *mélange* presence preferentially suppresses smaller events, but is relatively ineffective at holding back larger events, which will calve regardless once they become sufficiently unstable. The latter may reflect a limitation in the ability of the *mélange* buttressing force to suppress large calving events, i.e. once fracture propagation from the forward-rotating weight of the collapsing subaerial ice exceeds the closure imposed by *mélange* backstress. We note, however, that this limitation is specific only to our observations and that the *mélange* buttressing force could have been higher prior to the melt season when the weather was colder.

However, a calving front exhibiting self-organised critical behaviour near its critical point should show calving activity that follows a power-law distribution with exponents in the range 1.06-1.46 (Åström et al., 2014), which we do not observe in this study. On the other hand, we do observe qualitative changes in calving behaviour between a likely subcritical calving phase (5th-7th; dominated by smaller events), a likely supercritical phase (8th-14th; dominated by larger events) and a second subcritical phase (15th-27th; dominated by smaller events), with the period

Accepted Article

of subcriticality representing over 2/3 of the record duration. These features are consistent with a calving front operating in a self-organised critical regime (Åström et al., 2014). It is also worth noting that, for grounded tidewater margins, which is the relevant category for the northern part of Store's calving front, the power law is expected to display an exponential cut-off for calving events with volumes over 10^4 m^3 (Åström et al., 2014). If we only consider the events below this volume threshold and repeat the power-law analysis described in Sect. 4.1, we find R^2 values of 0.83, 0.77, and 0.78, respectively. These represent a significant improvement in R^2 values for the two putatively subcritical phases and little change for the putatively supercritical phase, which is consistent with grounded calving fronts operating in a self-organised critical regime (Åström et al., 2014). The power-law exponents, however, jump to 3.66, 3.73 and 3.64 when considering events below this 10^4 m^3 threshold, which is much higher than expected from Åström et al. (2014). We attribute this to our processing method excluding events below 4000 m^3 in size, distorting the tail of the distribution. However, we note that Walter et al. (2020) found a power-law exponent of 3.7 for the shallow section of the calving front of Eqip Glacier, and 2.3 for the deep section, with calving biased towards the smaller end of the size scale considered in our study, so our power-law exponents may not be overly distorted by the truncated tail. Therefore, we suggest that the calving front at Store exhibits behaviour that is at least qualitatively consistent with self-organised criticality and potentially provide quantitative support for this. This point also reinforces our assertion that calving behaviour changes over time and thus cannot be necessarily well-represented or modelled by a short time series of observations.

We additionally show that visible active meltwater plumes, driven by surface melt, encourage more frequent calving events (Figure 10b), possibly as a response to undercutting of the calving front, as described above. What is less intuitive is that the increase in the number of events is associated with barely any increase in the volume loss from calving. The presence of plumes in this study greatly increases the number of smaller ($<10^5 \text{ m}^3$) calving events at the expense of the larger events ($>10^5 \text{ m}^3$), which fall from 24% (representing 909 events) to 11% (representing 730 events) of the total event count. We attribute this to plume-induced melting making it 'easier' for blocks and small vulnerable sections of the front to break off, removing them consecutively in a relatively high number of events, which may reduce stresses in the ice, thereby reducing the frequency of large calving events. This does not, however, mean plumes reduce the total mass loss as we are unable to observe the quantity of ice lost by plume-induced melting, or calving, taking place below the waterline. The finding does, nonetheless, highlight that the relationship between plumes and calving is not as straightforward as previously proposed (O'Leary & Christoffersen, 2013; Mercenier et al., 2020).

Also, the bimodal distribution of iceberg sizes found in this study of Store shows that classification of glaciers into types that produce either small magnitude icebergs by serac failure or large icebergs by full-thickness capsizing slabs or tabular icebergs, with Store falling in the latter category according to Fried et al. (2018), may be too simplistic since both types of events are observed to occur frequently at Store. While it is possible that some glaciers will calve mostly by one mechanism and that others will calve mostly by the other, our TRI record from Store indicates that the calving mechanism inherently comprises both and that the predominant calving style can change from one type to the other over relatively short periods. This finding is a result of the extremely high resolution of the TRI, which recorded calving every 3 minutes. While our UAV investigation showed a subaerial volume loss of $1,404,000 \text{ m}^3$ from a frontal

retreat between two surveys separated by 12 hours (Figure 4), the TRI showed this retreat was comprised of 48 individual events and that iceberg sizes varied by two orders of magnitude or more (Figure 5). This finding indicates that there are inherent limitations in the use of remotely sensed images to discern calving styles and that classification of calving glaciers may require size-frequency distributions and assessment of probability (Figure 6, Figure 11).

5.3. Limitations and validation

This study has produced one of the longest records of calving from the use of a TRI. The instrument captured calving events occurring over half of the calving front of Store during three weeks in July 2017. Overall, we found a very good agreement between the volumetric loss of ice in a multitude of calving events with those estimated from the UAV-derived DEMs produced at a 0.2 m resolution (Figure 3, Figure 4). This gives us confidence that the TRI was successful in identifying calving events on the northern side of Store and that the TRI analysis has produced accurate volumetric estimates. However, due to the 5-km-wide calving front, it was not possible to also survey calving taking place in the southern half of the terminus, where numerical modelling indicates the largest, tabular-style calving events are most likely to occur (Todd et al., 2018). However, our study shows that the northern terminus is very close to floatation and thus that the differences between our observations and the floating southern half may not be so pronounced.

A fundamental limitation of the TRI is that it only observes subaerial calving volumes. As computed in Section 4.1, we find a nine times greater submarine calving volume than the subaerial volume from UAV and TRI DEMs for the sequence of calving events displayed in Figures 2 and 3. This shows that the northern calving front we observe is at or very close to floatation, and hence that the observed modal peak in the subaerial calving volume of larger events represents only 1/10th of the actual iceberg size. The modal peak of the smaller iceberg sizes may, however, be close to the actual volume given that these events represent relatively smaller blocks or slabs of ice falling off the front.

While the use of the TRI has provided a record of calving with unprecedented detail and resolution, the presence of radar shadows is a limitation that introduces inherent data gaps, i.e. when the coherence of the TRI returns are insufficient to extract elevation data. The effect of these on the dataset is to a) not detect small calving events that happen in the radar voids, and b) not detect the full size of large calving events that spread across a void. With an independent record of calving from contemporaneous UAV surveys, we estimate the error induced by these radar shadows to be around 12%. The main limitation to this study as a result of this error is a bias towards underestimating both small and large calving events. This error is small in comparison to the limitation associated with detection range, which restricts our study to the northern half of the terminus. To detect all calving events at Store in an absolute sense, multiple TRI instruments would be needed. These additional resources were not available in this study.

6 Conclusions

We present a novel 3-week-long record of calving events at Store Glacier from a TRI survey that includes the transition from a mélange-filled proglacial fjord setting to a mélange-free environment. The record includes a total of 8,026 calving events with a mean volume of 4.8 x

Accepted Article

10^4 m^3 . Maximum calving rates peak at 30 events per hour, or 720 per day, with an average rate of 17 events per hour, or 408 per day. This dataset suggests mélange presence preferentially suppresses smaller calving events and that mélange break-up leads to a prolonged period of higher calving activity at Store, with calving rates nearly doubling in open-water and mélange-free conditions. We assess the accuracy of this dataset by making a comparison with calving events independently and contemporaneously recorded across a 12-hour period between two UAV surveys. The UAV surveys show that radar shadowing may introduce a 12% error in the TRI-detected calving volume; however the TRI record shows that the single-volume change recorded by the UAV surveys actually represents 48 small calving events. With the TRI capturing calving events in high resolution, both spatially and temporally, we find a bimodal size-frequency distribution of events that reflects two specific types of calving: blocks and relatively small sections of ice breaking off the subaerial part of the terminus with a characteristic modal size of 10^4 m^3 , and much larger icebergs released from full-thickness failure. While the observed modal size of the latter is 10^5 m^3 , we estimate the actual volume to be closer to 10^6 m^3 since our observations capture only the subaerial portion of the terminus, which is at or near floatation. However, we find the predominant type of calving can change from small to large events over relatively short periods.

With both temporal and spatial variability in calving at Store, our observations do not support any simple power-law relationship between iceberg size and frequency. Instead, we observe a complex relationship between calving and the presence of visible meltwater plumes at the calving front. Plume presence leads to 70% more calving events, but the subaerial volume of ice detaching from the terminus in these events only increases by 3%. We relate this to reduced support due to plume-induced melting allowing unstable ice blocks to calve earlier than they might otherwise have done. We further find little relationship between surface melt and calving volumes, though a statistically significant one between surface melt and calving counts, again indicating the complexities underlying calving behaviour.

Acknowledgments, Samples, and Data

This research was supported by the European Research Council as part of the RESPONDER project funded under the European Union's Horizon 2020 research and innovation programme (grant agreement no. 683043). SJC and TRC were supported by Natural Environment Research Council Doctoral Training Partnership studentships (NE/L002507/1), and AA by the European Union's Horizon 2020 research and innovation programme under a Marie Skłodowska-Curie grant (grant agreement no. 705215). We are grateful to the 2017 RESPONDER field team for their assistance in the field, and to Ann Andreasen and the Uummannaq Polar Institute for their kind hospitality. We would also like to thank Fabien Gillet-Chaulet for allowing SJC time to continue working on the manuscript.

The data for this paper is available from the University of Cambridge's Apollo data repository at <https://doi.org/10.17863/CAM.50070>.

References

Amundson, J. M., & Truffer, M. (2010). A unifying framework for iceberg-calving models.

Journal of Glaciology, 56(199), 822–830. <https://doi.org/10.3189/002214310794457173>

- Aschwanden, A., Fahnestock, M. A., Truffer, M., Brinkerhoff, D. J., Hock, R., Khroulev, C., et al. (2019). Contribution of the Greenland Ice Sheet to sea level over the next millennium. *Science Advances*, 5(6), eaav9396. <https://doi.org/10.1126/sciadv.aav9396>
- Åström, J. A., Riikilä, T. I., Tallinen, T., Zwinger, T., Benn, D., Moore, J. C., & Timonen, J. (2013). A particle based simulation model for glacier dynamics. *The Cryosphere*, 7(5), 1591–1602. <https://doi.org/10.5194/tc-7-1591-2013>
- Åström, J. A., Vallot, D., Schäfer, M., Welty, E. Z., O’Neel, S., Bartholomäus, T. C., et al. (2014). Termini of calving glaciers as self-organized critical systems. *Nature Geoscience*, 7(12), ngeo2290. <https://doi.org/10.1038/ngeo2290>
- Bassis, J. N., & Jacobs, S. (2013). Diverse calving patterns linked to glacier geometry. *Nature Geoscience*, 6(10), 833–836. <https://doi.org/10.1038/ngeo1887>
- Benn, D. I., & Åström, J. A. (2018). Calving glaciers and ice shelves. *Advances in Physics: X*, 3(1), 1513819. <https://doi.org/10.1080/23746149.2018.1513819>
- Benn, D. I., Cowton, T., Todd, J., & Luckman, A. (2017). Glacier Calving in Greenland. *Current Climate Change Reports*, 1–9. <https://doi.org/10.1007/s40641-017-0070-1>
- Benn, D. I., Åström, J., Zwinger, T., Todd, J., Nick, F. M., Cook, S., et al. (2017). Melt-under-cutting and buoyancy-driven calving from tidewater glaciers: new insights from discrete element and continuum model simulations. *Journal of Glaciology*, 1–12. <https://doi.org/10.1017/jog.2017.41>
- Catania, G. A., Stearns, L. A., Sutherland, D. A., Fried, M. J., Bartholomäus, T. C., Morlighem, M., et al. (2018). Geometric Controls on Tidewater Glacier Retreat in Central Western Greenland. *Journal of Geophysical Research: Earth Surface*, 123(8), 2024–2038. <https://doi.org/10.1029/2017JF004499>

Chapuis, A., & Tetzlaff, T. (2014). The variability of tidewater-glacier calving: Origin of event-size and interval distributions. *Journal of Glaciology*, 60(222), 622–634.

<https://doi.org/10.3189/2014JoG13J215>

Chapuis, A., Rolstad, C., & Norland, R. (2010). Interpretation of amplitude data from a ground-based radar in combination with terrestrial photogrammetry and visual observations for calving monitoring of Kronebreen, Svalbard. *Annals of Glaciology*, 51(55), 34–40.

<https://doi.org/10.3189/172756410791392781>

Chudley, T. R., Christoffersen, P., Doyle, S. H., Abellan, A., & Snooke, N. (2019). High-accuracy UAV photogrammetry of ice sheet dynamics with no ground control. *The Cryosphere*, 13(3), 955–968. <https://doi.org/10.5194/tc-13-955-2019>

van Dongen, E., Jouvét, G., Walter, A., Todd, J., Zwinger, T., Asaji, I., et al. (2019). Tides modulate crevasse opening prior to a major calving event at Bowdoin Glacier, Northwest Greenland. *Journal of Glaciology*, 1–11. <https://doi.org/10.1017/jog.2019.89>

Fried, M. J., Catania, G. A., Stearns, L. A., Sutherland, D. A., Bartholomäus, T. C., Shroyer, E., & Nash, J. (2018). Reconciling drivers of seasonal terminus advance and retreat at thirteen central west Greenland tidewater glaciers. *Journal of Geophysical Research: Earth Surface*, 0(ja). <https://doi.org/10.1029/2018JF004628>

How, P., Schild, K., Benn, D., Noormets, R., Kirchner, N., Luckman, A., et al. (2018). Calving controlled by melt-under-cutting: detailed calving styles revealed through time-lapse observations. *Annals of Glaciology*. Retrieved from <https://doi.org/10.1017/aog.2018.28>

Jouvét, G., Weidmann, Y., Seguinot, J., Funk, M., Abe, T., Sakakibara, D., et al. (2017).

Initiation of a major calving event on the Bowdoin Glacier captured by UAV

photogrammetry. *The Cryosphere*, 11(2), 911–921. <https://doi.org/10.5194/tc-11-911-2017>

Mallalieu, J., Carrivick, J. L., Quincey, D. J., Smith, M. W., & James, W. H. M. (2017). An integrated Structure-from-Motion and time-lapse technique for quantifying ice-margin dynamics. *Journal of Glaciology*, 63(242), 937–949. <https://doi.org/10.1017/jog.2017.48>

Mercenier, R., Lüthi, M. P., & Vieli, A. (2020). How Oceanic Melt Controls Tidewater Glacier Evolution. *Geophysical Research Letters*, 47(8), e2019GL086769. <https://doi.org/10.1029/2019GL086769>

Morlighem, M., Bondzio, J., Seroussi, H., Rignot, E., Larour, E., Humbert, A., & Rebuffi, S. (2016). Modeling of Store Gletscher’s calving dynamics, West Greenland, in response to ocean thermal forcing. *Geophysical Research Letters*, 43(6), 2016GL067695. <https://doi.org/10.1002/2016GL067695>

Mouginot, J., Rignot, E., Bjørk, A. A., van den Broeke, M., Millan, R., Morlighem, M., et al. (2019). Forty-six years of Greenland Ice Sheet mass balance from 1972 to 2018. *Proceedings of the National Academy of Sciences*, 201904242. <https://doi.org/10.1073/pnas.1904242116>

O’Leary, M., & Christoffersen, P. (2013). Calving on tidewater glaciers amplified by submarine frontal melting. *The Cryosphere*, 7(1), 119–128. <https://doi.org/10.5194/tc-7-119-2013>

Pełlicki, M., & Kinnard, C. (2016). Calving of Fuerza Aérea Glacier (Greenwich Island, Antarctica) observed with terrestrial laser scanning and continuous video monitoring. *Journal of Glaciology*, 62(235), 835–846. <https://doi.org/10.1017/jog.2016.72>

- Podgórski, J., Pełlicki, M., & Kinnard, C. (2018). Revealing recent calving activity of a tidewater glacier with terrestrial LiDAR reflection intensity. *Cold Regions Science and Technology*, 151, 288–301. <https://doi.org/10.1016/j.coldregions.2018.03.003>
- Rignot, E., & Mouginot, J. (2012). Ice flow in Greenland for the International Polar Year 2008-2009: ICE FLOW GREENLAND 2009. *Geophysical Research Letters*, 39(11), n/a-n/a. <https://doi.org/10.1029/2012GL051634>
- Rignot, E., Xu, Y., Menemenlis, D., Mouginot, J., Scheuchl, B., Li, X., et al. (2016). Modeling of ocean-induced ice melt rates of five west Greenland glaciers over the past two decades. *Geophysical Research Letters*, 43(12), 2016GL068784. <https://doi.org/10.1002/2016GL068784>
- Strozzi, T., Werner, C., Wiesmann, A., & Wegmuller, U. (2012). Topography Mapping With a Portable Real-Aperture Radar Interferometer. *IEEE Geoscience and Remote Sensing Letters*, 9(2), 277–281. <https://doi.org/10.1109/LGRS.2011.2166751>
- Todd, J., & Christoffersen, P. (2014). Are seasonal calving dynamics forced by buttressing from ice mélange or undercutting by melting? Outcomes from full-Stokes simulations of Store Glacier, West Greenland. *The Cryosphere*, 8(6), 2353–2365. <https://doi.org/10.5194/tc-8-2353-2014>
- Todd, Joe, Christoffersen, P., Zwinger, T., Råback, P., Chauché, N., Benn, D., et al. (2018). A Full-Stokes 3D Calving Model applied to a large Greenlandic Glacier. *Journal of Geophysical Research: Earth Surface*, 2017JF004349. <https://doi.org/10.1002/2017JF004349>
- Todd, Joe, Christoffersen, P., Zwinger, T., Råback, P., & Benn, D. I. (2019). Sensitivity of a calving glacier to ice–ocean interactions under climate change: new insights from a 3-D

full-Stokes model. *The Cryosphere*, 13(6), 1681–1694. <https://doi.org/10.5194/tc-13-1681-2019>

Vallot, D., Adinugroho, S., Strand, R., How, P., Pettersson, R., Benn, D. I., & Hulton, N. R. J. (2019). Automatic detection of calving events from time-lapse imagery at Tunabreen, Svalbard. *Geoscientific Instrumentation, Methods and Data Systems*, 8(1), 113–127. <https://doi.org/10.5194/gi-8-113-2019>

van Wessem, J. M., Berg, W. J. van de, Noël, B. P. Y., Meijgaard, E. van, Amory, C., Birnbaum, G., et al. (2018). Modelling the climate and surface mass balance of polar ice sheets using RACMO2 – Part 2: Antarctica (1979–2016). *The Cryosphere*, 12(4), 1479–1498. <https://doi.org/10.5194/tc-12-1479-2018>

Voytenko, D., Dixon, T. H., Holland, D. M., Cassotto, R., Howat, I. M., Fahnestock, M. A., et al. (2017). Acquisition of a 3 min, two-dimensional glacier velocity field with terrestrial radar interferometry. *Journal of Glaciology*, 63(240), 629–636. <https://doi.org/10.1017/jog.2017.28>

Walter, A., Lüthi, M. P., & Vieli, A. (2020). Calving event size measurements and statistics of Eqip Sermia, Greenland, from terrestrial radar interferometry. *The Cryosphere*, 14(3), 1051–1066. <https://doi.org/10.5194/tc-14-1051-2020>

Werner, C., Strozzi, T., Wiesmann, A., & Wegmuller, U. (2008). A Real-Aperture Radar for Ground-Based Differential Interferometry. In *IGARSS 2008 - 2008 IEEE International Geoscience and Remote Sensing Symposium* (Vol. 3, pp. III-210–III-213). <https://doi.org/10.1109/IGARSS.2008.4779320>

Xie, S., Dixon, T. H., Holland, D. M., Voytenko, D., & Vaňková, I. (2019). Rapid iceberg calving following removal of tightly packed pro-glacial mélange. *Nature Communications*, *10*(1), 3250. <https://doi.org/10.1038/s41467-019-10908-4>

Xu, Y., Rignot, E., Fenty, I., Menemenlis, D., & Flexas, M. M. (2013). Subaqueous melting of Store Glacier, west Greenland from three-dimensional, high-resolution numerical modeling and ocean observations: SUBAQUEOUS MELTING OF STORE GLACIER. *Geophysical Research Letters*, *40*(17), 4648–4653. <https://doi.org/10.1002/grl.50825>

